Structural and electronic properties of β-$FeSi_2$ nanoparticles: The role of stacking fault domains

Robert Imlau,[1] András Kovács,[1,*] Ervin Mehmedovic,[2] Pengxiang Xu,[3] Andrew A. Stewart,[4,5] Christine Leidinger,[6] Rafal E. Dunin-Borkowski,[1] Gustav Bihlmayer,[3] Hartmut Wiggers,[2] Reinhard Carius,[6] Ute Kolb,[4,7] and Martina Luysberg[1]

[1]*Ernst Ruska-Centre for Microscopy and Spectroscopy with Electrons and Peter Grünberg Institute 5, Forschungszentrum Jülich, 52425 Jülich, Germany*

[2]*University of Duisburg-Essen, Institute for Combustion and Gasdynamics—Reactive Fluids and Center for Nanointegration Duisburg-Essen (CENIDE), 47057, Duisburg, Germany*

[3]*Institute for Advanced Simulation and Peter Grünberg Institut 1, Forschungszentrum Jülich, 52425 Jülich, Germany*

[4]*Institute for Physical Chemistry, Johannes Gutenberg-University, 55099 Mainz, Germany*

[5]*Department of Physics and Energy, University of Limerick, Castletroy, Ireland*

[6]*Institute of Energy- and Climate Research - Photovoltaics, Forschungszentrum Jülich, 52425 Jülich, Germany*

[7]*TU Darmstadt, Institut für Angewandte Geowissenschaften, 64287 Darmstadt, Germany*

(Received 19 November 2013; revised manuscript received 25 January 2014; published 24 February 2014)

We use conventional and aberration-corrected transmission electron microscopy (TEM) and *ab initio* calculations to investigate the structural and electronic properties of β-$FeSi_2$ nanoparticles, which are a promising material for photovoltaic applications due to a band gap of <1 eV and a high absorption coefficient. The nanoparticles have average sizes of $\sim$20 nm, form aggregates, and are prepared by gas-phase synthesis. Amorphous SiO_x shells with thicknesses of $\sim$1.7 nm around β-$FeSi_2$ cores are identified on individual nanoparticles using electron energy-loss spectroscopy, while stacking fault domains in the nanoparticles are observed using high-resolution TEM, nanobeam electron diffraction, and automated diffraction tomography. *Ab initio* calculations indicate only minor changes in band structure in the faulted structure when compared to perfect β-$FeSi_2$. The optical properties of imperfect β-$FeSi_2$ nanoparticles are therefore expected to be the same as those of the perfect structure, suggesting that β-$FeSi_2$ nanoparticles are suitable candidates for use in optical absorber layers in thin film solar cells.

DOI: 10.1103/PhysRevB.89.054104 PACS number(s): 81.07.Bc, 61.72.Ff, 31.15.A−

I. INTRODUCTION

Iron-disilicide, crystallized in the β phase (β-$FeSi_2$), has received considerable recent attention because of its advantageous thermoelectric and optical properties, which make it interesting for thermoelectric, as well as light-sensitive and light-emitting applications. Furthermore, β-$FeSi_2$ is nontoxic, consists of elements that are abundant in nature, and is compatible with existing silicon-based technology [1]. Optical experiments have revealed indirect and direct band gaps of 0.78 eV and 0.84 eV, respectively [2]. An absorption coefficient α of above 10^5 cm^{-1} has been reported for β-$FeSi_2$ thin films [3]. The β structure [4] is orthorhombic with space group *Cmca*; has lattice parameters $a = 0.986$ nm, $b = 0.779$ nm, and $c = 0.783$ nm; and forms in a narrow compositional range close to an Fe content [5] of 33.3 at.%. The crystal structure can be described in terms of a packing of deformed cubes, in which the Si atoms occupy the corners and the Fe atoms one of the two central sites.

The synthesis of β-$FeSi_2$ is relatively straightforward, involving the solid-state reaction of Si and Fe at elevated temperature to prepare the bulk material [6], a thin film [7], on Si or embedded nanocrystals [8] in Si. As lattice strain at the β-$FeSi_2$/Si interface changes the electronic structure and optical properties [9–12] of β-$FeSi_2$ significantly, the synthesis of free-standing β-$FeSi_2$ is highly attractive for light-sensitive applications. However, its fabrication has been a major issue to date using any physical or chemical deposition processes. Gas phase synthesis [13] of the nanocrystalline material is potentially a suitable preparation technique. However, the different reaction kinetics of the Fe and Si precursor gases have impeded its successful fabrication. Recently, Bywalez *et al.* [14] succeeded in the preparation of free-standing β-$FeSi_2$ nanoparticles (NPs) using chemical vapor synthesis in a hot wall reactor.

Here, we assess whether β-$FeSi_2$ NPs are suitable for use in optical absorber layers. This application requires that (i) the NPs are larger than about 15 nm to ensure sufficient optical absorption that is representative of bulklike electronic behavior rather than quantum confined electronic states and that (ii) structural, stoichiometric, compositional and electronic properties of the entire β-$FeSi_2$ NPs agree with those of the bulk material. We use a wide range of advanced transmission electron microscopy (TEM) techniques to investigate the atomic structures, morphologies, and chemical compositions of individual β-$FeSi_2$ NPs. The results we present benefit from the latest advances in TEM, including the development of aberration correctors for electron lenses that allow confined nanostructures to be studied with unprecedented resolution. Based on our experimental findings, we determine the band structures of β-$FeSi_2$ NPs using density functional theory (DFT) calculations, employing the generalized gradient approximation (GGA) for the exchange-correlation potential.

II. METHODS

β-$FeSi_2$ NPs were prepared by chemical vapor synthesis in a hot wall reactor using silane (SiH_4) and iron pentacarbonyl ($Fe(CO)_5$) as precursor gases. The choice of synthesis parameters, such as the ratio of reactive gases, the temperature, and the residence time within the reaction zone, was found to be

*Corresponding author: a.kovacs@fz-juelich.de

crucial for the fabrication of Fe-Si NPs in the desired β phase. Further details about the preparation of the NPs are reported elsewhere [14].

Specimens for TEM characterization were prepared directly from the pristine powder on lacey carbon-coated Cu grids without using organic solvents. Standard imaging and diffraction studies were performed using an FEI Tecnai G2 microscope operated at an accelerating voltage of 200 kV. The phase composition of the nanocrystals was determined using selected area electron diffraction (SAED) patterns recorded on a 2 k × 2 k charged coupled device camera, with the camera length calibrated using the positions of diffraction spots from an Au film deposited onto part of the β-$FeSi_2$ sample.

The crystallographic structure of the β-$FeSi_2$ NPs was also studied using nanobeam electron diffraction (NBED) combined with automated diffraction tomography (ADT) [15] in microprobe scanning TEM (STEM) mode using a 10-μm condenser aperture. Annular dark-field (ADF) STEM images were recorded during the acquisition of ADT series to ensure that NBED patterns were obtained from the same β-$FeSi_2$ nanocrystal over a specimen tilt range of $\pm 60°$, which was acquired in 1° increments using a Fischione dual-axis tomography holder. The diffraction data were collected using a 30-nm electron beam; a smaller beam diameter was not possible in this geometry without introducing significant distortions. The electron diffraction dataset was processed using ADT3D software (Nanomegas, Belgium) in conjunction with Matlab scripts [16]. UCSF Chimera software was used for visualization of the three-dimensional (3D) datasets [17].

For high-resolution TEM (HRTEM) studies, an image aberration-corrected FEI Titan 80-300 microscope was used at an accelerating voltage of 300 kV with the aberration functions of the imaging system corrected to fourth order. The spherical aberration coefficient (C_s) of the objective lens was adjusted to be slightly negative in order to enhance the contrast [18] in the TEM images. Atomic positions were inferred from aberration-corrected TEM images by making use of multislice simulations of the images performed using the Java version of an EMS computer program [19].

The chemical distribution of the elements within individual β-$FeSi_2$ NPs was studied using electron energy-loss spectroscopy (EELS) combined with ADF imaging and probe aberration-corrected STEM in an FEI Titan 80-300 microscope operated at 300 kV. The StripeSTEM [20] EELS technique was used to reduce electron beam damage during the acquisition of EELS spectra.

Energy-filtered TEM (EFTEM) studies of the nanocrystals were performed using a C_s and chromatic (C_c) aberration-corrected FEI Titan 60-300 microscope. An accelerating voltage of 80 kV was used to minimize the effect of electron beam irradiation on the structure of the β-$FeSi_2$ NPs during prolonged EFTEM studies. The value of C_c was reduced to $\sim$5 μm to allow EFTEM elemental maps to be recorded with a spatial resolution of better than 0.2 nm. Spatial drift in the image series was corrected using a statistically determined spatial drift correction program [21]. DigitalMicrograph software (Gatan) was used for image processing.

Simulations of the electronic properties of the β-$FeSi_2$ nanocrystals were performed using DFT calculations employing the GGA as proposed by Perdew *et al.* [22]. We used the full-potential linearized augmented plane-wave (FLAPW) method, as implemented in the FLEUR code (www.flapw.de). Basis functions with a reciprocal lattice cut-off vector K_{max} of 3.7 $(a.u.)^{-1}$ were included. Self-consistency was considered to have been achieved when the total energy variation between iterations did not exceed 3×10^{-5} eV and forces on the atoms had converged to 50 meV/Å. Increasing the plane-wave cutoff K_{max} to 4.0 $(a.u.)^{-1}$, we found that the changes of the total energy differences are also in the range of 3×10^{-5} eV. Reciprocal space was sampled by a mesh containing 75 **k** points [corresponding to an $(8 \times 8 \times 8)$ Monkhorst-Pack mesh] in the irreducible wedge of the Brillouin zone for the ideal bulk phases. Imperfect structure models containing stacking fault domains, which were derived from experimental observations, were treated using an equivalently dense **k**-point sampling. For structural optimization of these models, the lattice constants were constrained to the optimised bulk values for β-$FeSi_2$, and the atomic positions in the unit cell were allowed to relax. The relaxed lattice constants are $a = 0.983$ nm, $b = 0.781$ nm, and $c = 0.785$ nm.

III. STRUCTURAL AND CHEMICAL PROPERTIES

Figure 1(a) shows a bright-field (BF) TEM image of aggregated β-$FeSi_2$ NPs deposited on a lacey carbon film that is visible in the lower right corner of the image. The nanocrystals can be seen to have sintered together during synthesis into chainlike structures. The individual crystals are randomly oriented and overlap each other such that the different orientations and thickness changes give rise to contrast variations visible in the image of the nanocrystals. An average nanocrystal size of $\sim$20 nm was estimated by fitting irregular round shapes to their outlines, as shown in Fig. 1(a). At the underfocus imaging conditions used, a shell surrounding the NPs is revealed as a bright rim. The shell has an average thickness of 1.7 ± 0.4 nm, is amorphous, and consists of Si and O (see below). It was found that the shell is sensitive to electron beam irradiation, as its thickness decreased to 1–2 monolayers after irradiating the nanocrystals with an electron dose of $\sim$1000 e/pm^2 at an accelerating voltage of 200 kV. The shell regrew when the nanocrystals were exposed to air.

The crystallographic structure of the nanocrystals was confirmed to be orthorhombic β-$FeSi_2$ using SAED by comparing measured reciprocal lattice distances with structure models obtained from the literature [4]. An SAED pattern recorded from the aggregate in Fig. 1(a) is shown in Fig. 1(b). No texture or preferential crystallographic orientation in the nanocrystalline aggregates was observed. The peak positions in the diffraction patterns are consistent with those obtained from macroscopic x-ray diffraction (XRD) measurements [14] and with expected values for the β-$FeSi_2$ phase.

Aberration-corrected HRTEM images in combination with multislice image simulations were used to identify the locations of Fe and Si atomic columns near the nanocrystals surfaces. An HRTEM image of a β-$FeSi_2$ nanocrystal viewed along [011] is shown in Fig. 1(c) and displays a characteristic flowerlike pattern of bright spots, which is associated with individual Fe and Si columns. The image was recorded $\sim$10 nm underfocus and was selected from a through-focus series that contained both under- and overfocused images. A simulated

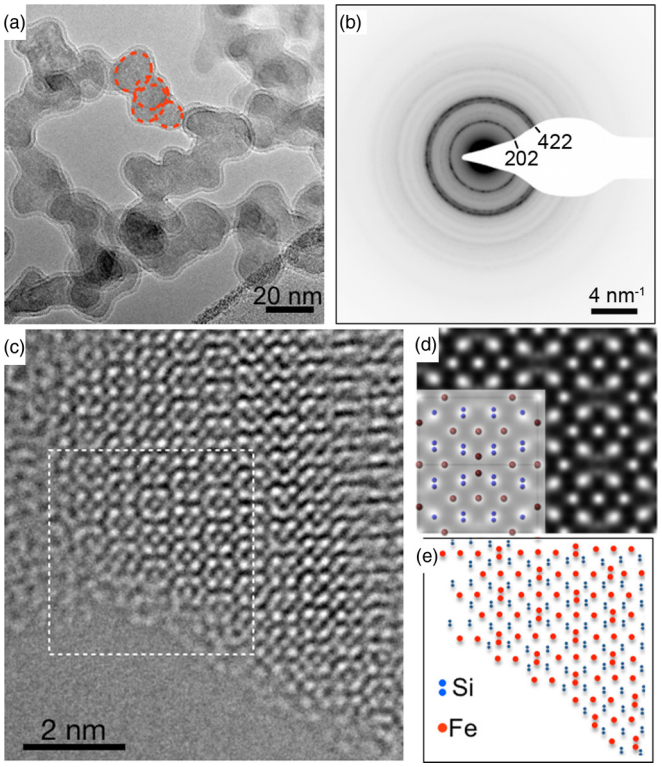

FIG. 1. (Color online) (a) Underfocused BF TEM image showing a nanocrystalline aggregate of β-$FeSi_2$ NPs revealing a shell surrounding the crystalline cores. The NPs in the aggregate are each ~20 nm in size, as marked by red dashed circles. (b) SAED pattern acquired from the β-$FeSi_2$ NPs corresponding to a random orientation of the nanocrystals. (c) Aberration-corrected HRTEM image of the edge of a β-$FeSi_2$ crystal. (d) Model of the β structure overlayed onto a multislice simulated HRTEM image. The red and blue colors correspond to Fe and Si atomic columns, respectively. For the simulation, an accelerating voltage of 300 kV, a [110] sample orientation, a C_s of -20 μm, an f of -12 nm, and a t of 4.4 nm were used. (e) Locations of Fe and Si atomic columns corresponding to the marked region of the experimental image shown in (c).

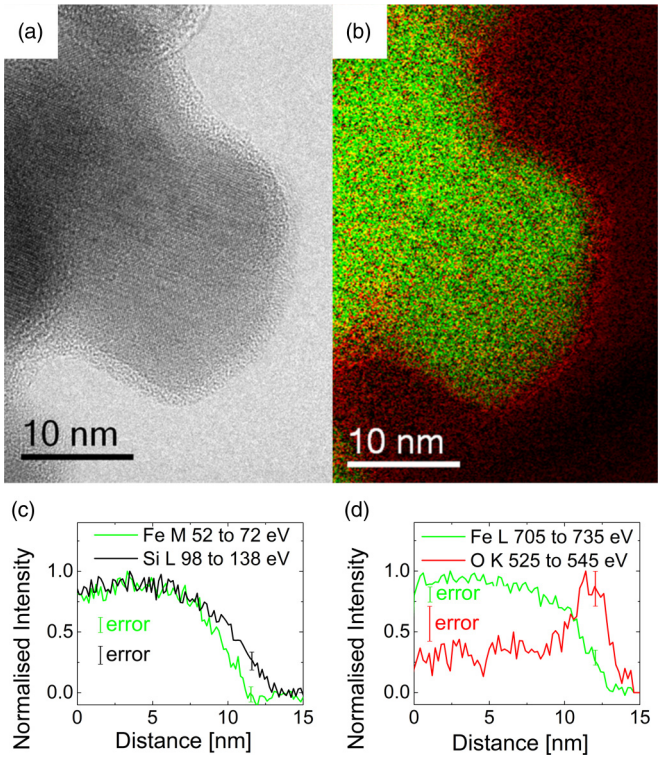

FIG. 2. (Color online) (a) BF TEM image showing a crystalline core and an amorphous shell on a β-$FeSi_2$ nanocrystal that was used for EFTEM. (b) False colored Fe L edge (green) and O K edge (red) EFTEM elemental maps recorded from the same nanocrystal using C_s- and C_c-corrected TEM at 80 kV. (c) and (d) Integrated intensity profiles of the background-subtracted (c) Fe M-edge and Si L-edge and (d) Fe L-edge and O K-edge EELS signals measured across the edge of a β-$FeSi_2$ NP.

HRTEM image, which incorporates values of $C_s = -20$ μm, defocus $f = -12$ nm, and specimen thickness $t = 4.4$ nm reproduces the experimental image very well, as shown in Fig. 1(d). The Si and Fe atomic column positions shown in Fig. 1(e) are inferred from the marked region in Fig. 1(c). The arrangement of Fe and Si atomic columns near the particle's crystalline surface reveals no distinct faceting, with the surface containing both Fe and Si atomic columns in stoichiometric composition.

EELS was used to measure local variations in chemical composition within the β-$FeSi_2$ NPs and the surrounding amorphous shell. In order to record EFTEM maps, an accelerating voltage of 80 kV was chosen to reduce electron beam-induced damage during acquisition because preliminary TEM studies performed at 200 kV revealed beam sensitivity of the shell. Despite the low accelerating voltage, a high spatial resolution of <0.2 nm could be achieved by correcting for both the spherical and the chromatic aberration of the microscope objective lens. Figures 2(a) and 2(b) show a BF TEM image and a corresponding Fe and O map, respectively, of a β-$FeSi_2$ NP. The Fe signal is confined to the core of the crystal, while significant O enrichment is observed in the shell. For elemental mapping, an energy range from 440 to 780 eV, an energy-selecting window size of 20 eV, and a step size of 20 eV were used, encompassing the K edge of O at 532 eV and the L edge of Fe at 709 eV. Unfortunately, a slight reduction in the thickness of the amorphous shell was observed after acquisition; therefore, a subsequent Si map could not be recorded from the same particle.

Elemental analysis of the nanocrystals using the StripeSTEM EELS technique was performed at 300 kV. In this technique, an isochronous recording of EELS spectra and ADF intensity provides spectroscopic information with a distributed dose on the sample. Despite the higher accelerating voltage used in the StripeSTEM experiments compared to the EFTEM experiments, no significant shell-thickness reduction was observed, probably due to the shorter acquisition time used. Figure 2(c) shows lateral profiles of the resulting background-subtracted EELS signals of the Fe M edge at 54 eV and the Si L edge at 99 eV measured from the center of a β-$FeSi_2$ particle to its surface. Within the particle, the Fe/Si ratio stays constant. Toward its edge, the Fe signal drops first, followed by the Si signal. The distance between the decreases in intensity is ~2 nm. The distribution of O and Fe was measured in the same way using the Fe L edge and O K edge, as shown in Fig. 2(d).

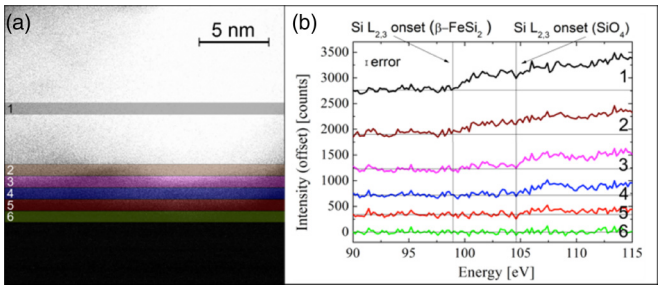

FIG. 3. (Color online) (a) HAADF STEM image of the edge of a β-$FeSi_2$ NP recorded during StripeSTEM EELS acquisition. (b) Background-subtracted EELS spectra of the edge region, showing a shift in Si $L_{2,3}$-edge onset. Numbers in (a) and (b) correspond to the individual spectra.

The O signal was constant in the middle of the nanocrystal and increased toward its surface, as expected for an O-rich shell. It can therefore be concluded that the amorphous shell observed on the surfaces of the β-$FeSi_2$ nanocrystals is rich in Si and O. However, the presence of a small amount of Fe in the shell cannot be completely excluded. Within the margin of error, the Fe/Si ratio stays constant across the NPs, indicating a homogeneous chemical composition of the core.

The electron-loss near-edge structure of the Si $L_{2,3}$ edge was used to obtain information about the density of unoccupied states of the Si bonds and to probe the Si bonding states, as discussed by Garvie and Buseck [23]. Figure 3 shows an ADF STEM image of the edge of a β-$FeSi_2$ nanocrystal and corresponding background-subtracted Si $L_{2,3}$ edges acquired from the core of the crystal, from the shell region, and from vacuum. The onset of the Si $L_{2,3}$ edge in the core of the crystal is at ~99 eV, while in the shell region it is shifted to ~104 eV, in good agreement with the expected onsets of the Si $L_{2,3}$ edge of crystalline Si [24] (99 eV) and of amorphous SiO_2 [23] (104.8 eV), in which the tetrahedra formed from Si and O bonds lack long-range order. Thus, the observed shift in the Si edge onset suggests that the shell structure is mostly SiO_x. Erlesand and Östling [25] showed that the presence of a surface oxide on β-$FeSi_2$ can be detrimental for current transport; therefore, it is recommended to avoid or to remove the oxide shell before implementing the NPs into a solar cell.

Following the deposition process, XRD was used to identify the phase of the nanocrystals as β-$FeSi_2$. However, the measured XRD spectra revealed reduced intensities of the (221), (312), and (421) peaks relative to the structure model of bulk β-$FeSi_2$ reported by Dusausoy *et al.* [4]. Based on their XRD and electron diffraction studies of bulk β-$FeSi_2$, Yamane and Yamada [6] proposed that the reduced intensities result from the presence of stacking faults associated with the slip system (100)[110]/2. The presence of a high density and the intrinsic behavior of such defects in β-$FeSi_2$ thin films was also reported by Zheng *et al.* [26]. The formation of stacking faults on successive lattice planes, resulting in stacking fault domains, is equivalent to exchanging the b and c axes of the material if the 0.5% difference in the two lattice parameters can neglected.

The examination of a large number of HRTEM images confirmed the presence of planar defects in the β-$FeSi_2$ NPs. Figure 4(a) shows a HRTEM image and a digital diffractogram

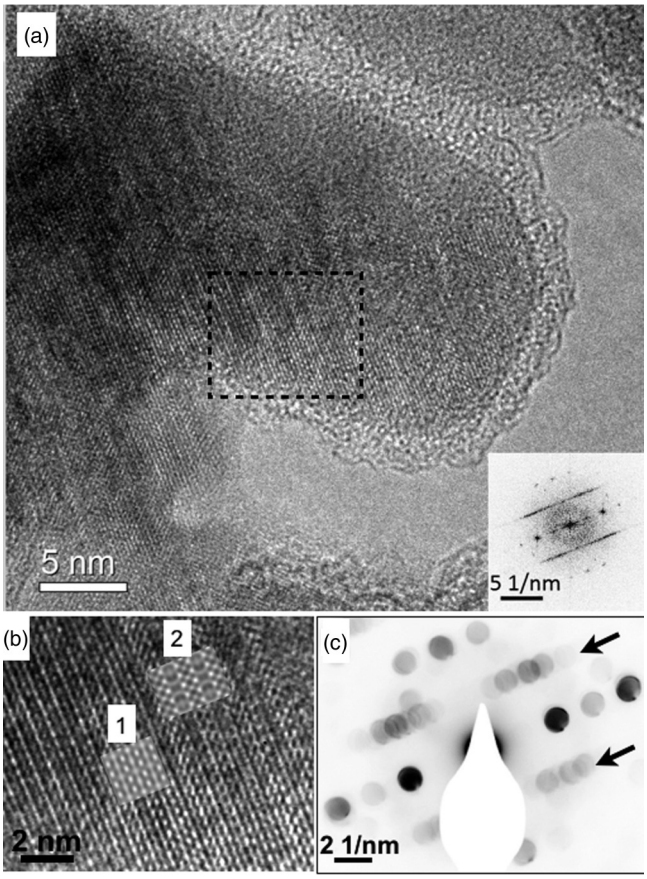

FIG. 4. (a) HRTEM image showing planar faults in β-$FeSi_2$ NPs. Inset is a digital diffractogram calculated from the image of the nanocrystal. (b) Magnified region of the HRTEM image marked in (a). The insets show simulated images of β-$FeSi_2$ viewed along (1) [021] and (2) [012]. (c) NBED pattern recorded from the nanocrystal shown in (a). Arrows mark lines of reflections visible at $k + l \neq 2n$ conditions.

generated from the imperfect region of the crystal. Streaks in the diffractogram are observed to extend perpendicular to the planar faults, which are associated with a stripelike contrast variation in the image. Figure 4(b) shows a magnified region of the HRTEM image, in which two contrast patterns are revealed, indicating the presence of two different stacking sequences. The insets show simulated images of β-$FeSi_2$ viewed along [012] and [021] directions and provide a good qualitative match to the experimental contrast. The image suggests that the NP contains both perfect regions and stacking fault domains, which are described in detail in Fig. 6. The domains are also revealed in an NBED pattern, which is shown in Fig. 4(c) and was recorded from the same β-$FeSi_2$ nanocrystal, as shown in Fig. 4(a), using a beam diameter of ~1 nm. Interestingly, the indexing of the NBED pattern could not be done unambiguously due to streak formation at every second row of reflections. The viewing direction was determined to be a superposition of both the [012] and [021] direction of β-$FeSi_2$.

Since the HRTEM image in Fig. 4 is a projection of a 3D structure and the conventional NBED pattern acquired from a β-$FeSi_2$ nanocrystal did not provide sufficient information about the planar defect, an ADT [15] experiment was performed on a β-$FeSi_2$ nanocrystal by collecting a tilt series of

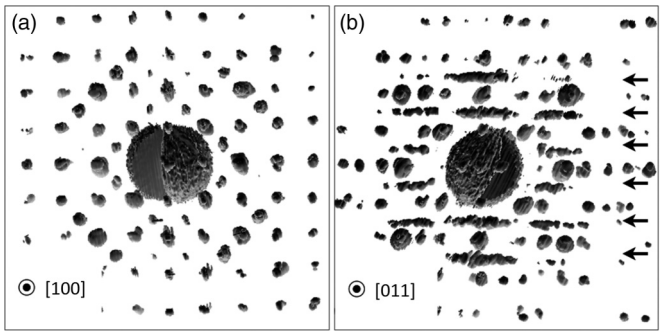

FIG. 5. Reconstructed three-dimensional reciprocal space intensity distribution acquired from a single β-$FeSi_2$ crystal and viewed along (a) [100] and (b) [011]. (b) Arrows mark lines of closely spaced reflections in every second row.

NBED patterns about an arbitrary specimen tilt axis in 1° increments over a range of ±60°. Figure 5(a) shows the resulting reconstructed 3D reciprocal space intensity distribution, viewed along the [100] direction, obtained from a single β-$FeSi_2$ NP. By tilting the reciprocal space intensity distribution to the orthogonal [011] direction, lines of closely spaced reflections could be observed along every second row, corresponding to hkl values of $k + l \neq 2n$, as shown in Fig. 5(b). The extinction criterion for visibility of the domains is therefore $\boldsymbol{g}\cdot\boldsymbol{R} \neq 2n$ where $\boldsymbol{g} = hkl$ are the Miller indices and $\boldsymbol{R} = [011]/2$ is the displacement vector. This extinction criterion is in agreement with that published by Yamane and Yamada [6], who reported the formation of (100)[011]/2 stacking faults, suggesting that the same type of defect is present in our nanocrystals.

IV. ELECTRONIC PROPERTIES AND DISCUSSION

The influence of the experimentally observed stacking fault domains on the electronic structure of β-$FeSi_2$ was investigated by performing *ab initio* calculations of the band structure. The domain structures were included in the models by adding a set of stacking fault layers that differs by a shift vector of (100)[011]/2 onto the same number of ideal $c(2 \times 2)$ $FeSi_2$ unit cells. Along the [100] direction, stacking fault layers were inserted into the ideal structure at different positions, as shown in Fig. 6(a). A stacking fault domain consisting of (100)[011]/2 stacking faults on successive lattice planes is shown in Fig. 6(c). Different domain models were considered and the most stable ones were identified by comparing their total energies. Models I and II assume two (100)[011]/2 stacking faults per unit cell forming a stacking fault domain. In Model I, the domain boundary is positioned at $a = ¾$, whereas in Model II the domain starts at $a = ¼$. Since Model I and II look similar in the projection displayed in Fig. 6(b), only Model I is shown. Figure 6(d) shows Model III, which contains one (100)[011]/2 stacking fault per unit cell.

After relaxation, the total energy of the most energetically favorable domain structure is ~42 meV per $c(2 \times 2)$ in-plane unit cell higher than that of an ideal structure with the same number of atoms (Table I). Constrained bulk calculations indicate that interchanging the b and c axes introduces a strain of ~40 meV [per $c(2 \times 2)$ in-plane unit cell]. Thus, the domain formation energy is small. Although more

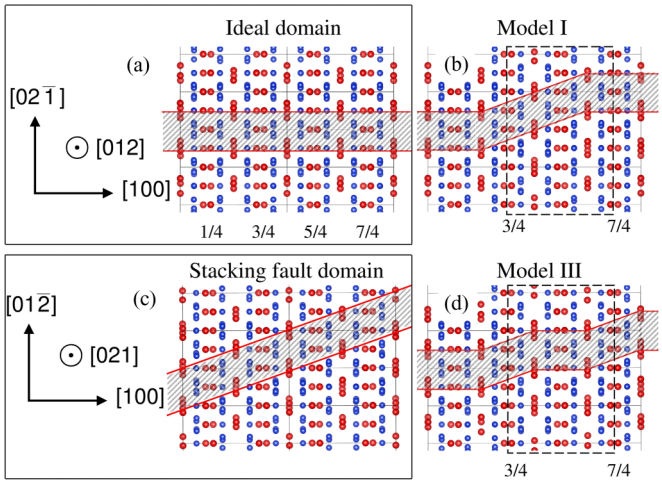

FIG. 6. (Color online) Two possible domains (Model I and Model III) used in *ab initio* calculations, where Fe is red and Si is blue. For ease of comparison, two unit cells are plotted along the a axis for each structure (shaded areas are a guide to the eye). (a) Ideal crystal structure of β-$FeSi_2$ viewed along [012]. (b) Model I: domain boundary between an ideal domain (a) and a stacking fault domain (c). The dashed box shows a stacking fault domain starting at $a = ¾$ unit cells. (c) Stacking fault structure of β-$FeSi_2$ viewed along [021]. (d) Model III: domain boundary between an ideal domain and a stacking fault domain, with only one stacking fault per unit cell, as shown in the dashed box.

complex low energy stacking faults cannot be excluded by our calculations, the small formation energy and the experimental evidence suggest that the studied configurations are the most important ones in this material.

In the case of a thin domain (1 + 1), two domain boundary planes are present with one unit cell distance. The thicker domains (2 + 2) also contain only two domain boundaries but with a two unit cell distance. The longer distance allows strain relaxation, reducing the formation energy by 1 meV for Models I and II, which have very similar formation energies. If less than two stacking faults per unit cell are present, as in Model III, then the formation energy is increased significantly. We can therefore conclude that, under equilibrium growth conditions, a single (100)[011]/2 stacking fault per unit cell will not form. The investigated crystallographic defects should therefore be referred to as stacking fault domains rather than (100)[011]/2 stacking faults.

In order to study the effect of the presence of stacking fault domains on the electronic properties of β-$FeSi_2$ NPs, the band structure of β-$FeSi_2$ was calculated. Sizable changes in direct transition energies induced by lattice deformations in

TABLE I. Formation energy (in units of meV per $c(2 \times 2)$ in-plane unit cell) from the three possible domains with different domain thicknesses. 1 + 1 means a stack of one ideal domain and one domain containing stacking faults. 2 + 2 refers to a stack of two ideal and two fault-containing domains.

	Model I	Model II	Model III
1 + 1	43	43	188
2 + 2	42	42	183

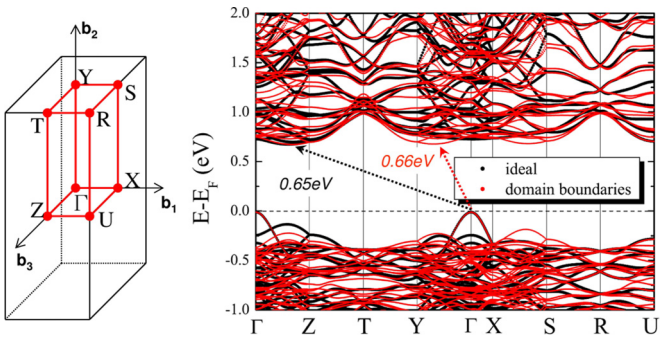

FIG. 7. (Color online) Band structures of β-$FeSi_2$ calculated with (red) and without (black) domain boundaries. As the unit cell was doubled in the [100] direction, the bands are folded back in the Γ-X direction.

the epitaxial β-$FeSi_2$/Si system have been reported in several studies [10–12]. However, to the best of our knowledge, the effect of (100)[011]/2 domain boundaries on the band structure has not been studied to date. Models of β-$FeSi_2$ with different concentrations of planar defects, as shown in Fig. 6, were investigated. Figure 7 displays the band structures of β-$FeSi_2$ calculated with and without domain boundaries (according to Model I), indicating only minor changes, such as a slightly larger band gap.

Most importantly, we see that the band character of the states forming the band gap has not been changed (Si-3p $\rightarrow$ Fe-3d) so that the absorption properties should not be strongly affected by the presence of the stacking fault domains.

In order to make use of the beneficial bulk properties of β-$FeSi_2$, which make this material a promising optical absorber, its structural and electronic properties should ideally be retained (or enhanced) when it is in NP form. This requirement applies not only to the crystal structure itself but also to the local chemical compositions of the NPs. In a recent paper, we demonstrated that the gas phase reactions that take place during preparation in a hot wall reactor can be well controlled, although the kinetics of the precursors silane and iron pentacarbonyl differ considerably [14]. As a result, the production of phase-pure β-$FeSi_2$ NPs was demonstrated.

As they have an average diameter of 20 nm, the present NPs should show bulklike electronic properties because their size exceeds the de Broglie wavelength $\lambda = h/\sqrt{2\mu_e^* kT} =$ 15.6 nm, below which quantum confinement occurs, where $\mu_e^* = 2.28\ 10^{-31}$ kg denotes the effective mass in the Γ-X direction calculated from the band structure, h is the Planck constant, k is the Boltzmann constant, and T is the absolute temperature (room temperature here). The fact that the NPs form aggregates is not expected to result in any detrimental effect on the absorbance. Except for the amorphous shell, no indications of compositional variations within or at the edges of the NPs were found, either using EELS or from HRTEM studies, in which Fe and Si atomic columns were observed to extend to the edges of the crystalline particles. Hence, our β-$FeSi_2$ NPs are of high quality in terms of size, stoichiometry, and phase purity.

The results presented here also reveal that the particles are imperfect in two aspects: (i) they have amorphous SiO_x-rich shells, and (ii) they contain structural defects, i.e., distinct crystallographic domains. The effect of the amorphous shell and of the domain structure on the optical properties needs to be addressed if they are to be used in applications.

The use of a β-$FeSi_2$ absorber layer in a solar cell requires efficient collection of charge resulting from the absorption of photons by the β-$FeSi_2$ NPs. Therefore, any possible barrier inhibiting charge transfer from the particle into the surrounding matrix, such as the observed amorphous SiO_x layer, should be avoided. We assume that the shell forms due to the adsorption of excess silane in the hot wall reactor onto the NPs. When exposed to air, the silane decomposes and forms SiO_x. We are currently investigating several routes to remove this layer, for example, by collecting the NPs under inert gas conditions and by using post-treatment, e.g., annealing.

As previously reported [6] for thin films, stacking fault domains are commonly formed in β-$FeSi_2$. They are also present in the particles investigated here, although the growth conditions differ considerably from those reported in the literature before. We have demonstrated the presence of domains within β-$FeSi_2$ NPs using various methods, including HRTEM, reciprocal space tomography, electron diffraction, and XRD. In order to understand the impact of these defects on the optical properties, *ab initio* calculations were performed based on several possible atomistic models of the domains. Affirmatively, the minimum energy configuration was consistent with the experimental observations, as shown in Figs. 6 and 4, respectively. Only minor changes in band structure between the perfect and imperfect crystalline structures were found. This result implies that, despite the presence of structural defects, β-$FeSi_2$ NPs are likely to be well suited for application in optical absorber layers.

V. CONCLUSIONS

In conclusion, phase-pure β-$FeSi_2$ NPs have been prepared using gas phase synthesis. We employed various conventional and advanced spectroscopic and imaging techniques to investigate the structures and compositions of the NPs down to the atomic scale. Aggregated β-$FeSi_2$ nanocrystals with sizes of $\sim$20 nm were found to be surrounded by amorphous SiO_x shells. Domains of successive stacking fault layers were observed on (200) planes. *Ab inito* calculations confirmed that the experimentally observed domain structures correspond to minimum energy configurations. Only minor changes in band structure are predicted for the faulted structures as compared to the perfect material. Hence, our β-$FeSi_2$ nanocrystals produced from the gas phase are expected to show the same optical properties as the bulk material and are expected to be well suited for use in optical absorber layers, e.g., in photovoltaic devices.

ACKNOWLEDGMENTS

This work was supported by a grant from the BMF under Contract No. 03SF0402A. T. Schena and L. Houben are acknowledged for valuable discussions. P.X. and G.B. are grateful for computing time on the JUROPA supercomputer at the Jülich Supercomputing Centre (JSC). A.S. and U.K. are grateful to the Deutsche Forschungsgemeinschaft (DFG) for support within the priority program 1415 Kristalline Nichtgleichgewichtsphasen.

[1] D. Leong, M. Harry, K. J. Reeson, and K. P. Homewood, Nature **387**, 686 (1997).
[2] K. Radermacher, O. Skeide, R. Carius, J. Klomfaß, and S. Manti, MRS Proceedings **320**, 115 (1993).
[3] M. C. Bost and J. E. Mahan, J. Appl. Phys. **58**, 2696 (1985).
[4] P. Y. Dusausoy, J. Protas, R. Wandji, and B. Roques, Acta Crystallogr. B **27**, 1209 (1971).
[5] Binary alloy phase diagram, ed. T. B. Massalski, ASM international 1108, (1987).
[6] H. Yamane and T. Yamada, J. Alloy Comp. **476**, 282 (2009).
[7] H. F. Liu, A. Huang, and D. Z. Chi, J. Appl. Phys. **109**, 083538 (2011).
[8] J. H. Won, A. Kovacs, M. Naito, M. Ishimaru, and Y. Hirotsu, J. Appl. Phys. **102**, 103512 (2007).
[9] Y. Terai, K. Noda, K. Yoneda, H. Udono, Y. Maeda, and Y. Fujiwara, Thin Solid Films **519**, 8468 (2011).
[10] D. B. Migas and L. Miglio, Phys. Rev. B **62**, 11063 (2000).
[11] H. Lange, Thin Solid Films **381**, 171 (2001).
[12] S. Eisebitt, J. E. Rubensson, M. Nicodemus, T. Böske, S. Blügel, W. Eberhardt, K. Radermacher, S. Mantl, and G. Bihlmayer, Phys Rev. B **50**, 18330 (1994).
[13] H. Hahn, Nanostruct. Mater. **9**, 3 (1997).
[14] R. Bywalez, H. Orthner, E. Mehmedovic, R. Imlau, A. Kovacs, M. Luysberg, and H. Wiggers, J. Nanopart. Res. **15**, 1878 (2013).
[15] U. Kolb, E. Mugnaioli, and T. E. Gorelik, Cryst. Res. Technol. **46**, 542 (2011).
[16] U. Kolb, T. Gorelik, C. Kübel, M. T. Otten, and D. Hubert, Ultramicroscopy **107**, 507 (2007); U. Kolb, T. Gorelik, and M. T. Otten, *ibid*. **108**, 763 (2008).
[17] E. F. Pettersen, T. D. Goddard, C. C. Huang, G. S. Couch, D. M. Greenblatt, E. C. Meng, and T. E. Ferrin, J. Comput. Chem. **13**, 1605 (2004).
[18] C. L. Jia, L. Houben, A. Thust, and J. Barthel, Ultramicroscopy **110**, 500 (2010).
[19] P. Stadelmann, Ultramicroscopy **21**, 131 (1987).
[20] M. Heidelmann, J. Barthel, and L. Houben, Ultramicroscopy **109**, 1447 (2009).
[21] B. Schaffer, W. Grogger, and G. Kothleitner, Ultramicroscopy **102**, 27 (2004).
[22] J. P. Perdew, K. Burke, and M. Ernzerhof, Phys. Rev. Lett. **77**, 3865 (1996).
[23] L. A. J. Garvie and P. R. Buseck, Amer. Mineral. **84**, 946 (1999).
[24] H. Matsumoto, S. Nagamatsu, M. Nakazawa, and T. Fujikawa, Physica Scripta **115**, 1099 (2005).
[25] U. Erlesand and M. Östling, Appl. Phys. Lett. **68**, 105 (1996).
[26] Y. Zheng, A. Taccoen, and J. F. Petroff, J. Appl. Crystall. **25**, 122 (1992).